IoT Platform Enhanced With Neural Network for Air Pollutant Monitoring

Alejandro Santos-Betancourt, José Carlos Santos-Ceballos, Foad Salehnia, Mohamed Ayoub Alouani, Alfonso Romero, José Luis Ramírez, and Xavier Vilanova

***Abstract*— This work presents the design and setup of an IoT platform at level four of the technology readiness level (TRL-4) to detect, classify, and quantify pollutant gases. This study combines concepts such as wireless sensor networks (WSNs), arrays of sensors, and multivariate data analysis to interface different nanostructured chemiresistor gas sensors. The IoT platform consists of several gas sensor nodes (GSNs) with Wi-Fi capability to send data from a sensor array to a server and its user interface (UI). Each GSN interfaces one sensor array (up to four chemiresistor gas sensors and one temperature and humidity sensor). The server channels the data from the GSNs to the UI. The platform was set up following a two-stage methodology. First (training stage), sensor data were received, stored, and used to train different multilayer perceptrons (MLPs) artificial neural networks (ANNs). Second (recognition stage), models were implemented in the UI to classify and quantify the presence of pollutants. The platform was tested in laboratory conditions under exposure to nitrogen dioxide and ammonia at a different %RH. As a result, the platform improves the classification and quantification times compared with the single-sensor approach. In addition, the system was evaluated using a gas mixture of both gases, showing a classification accuracy exceeding 99%. Likewise, the training and recognition stages can be repeated to add new chemiresistor gas sensors in the node, add new nodes to the platform, and deploy the nodes in different scenarios.**

***Index Terms*— Air pollution monitoring, ammonia, gas sensor, IoT, laboratory-made sensors, mixture of gases, multilayer perceptron (MLP), multivariate analysis, nitrogen dioxide.**

Received 29 August 2024; accepted 30 September 2024. Date of publication 16 October 2024; date of current version 5 November 2024. This work was supported in part by the EU in the framework of H2020-MSCA-RISE-2018: Marie Sklodowska-Curie Actions under Grant 823895-PE, in part by the Ministerio de Ciencia e Innovación (MICINN) under Grant PDC2022-133967-I00 and Grant TED2021-131442B-C31, and in part by the AGAUR under Grant 2021 SGR 00147. The work of Alejandro Santos-Betancourt was supported in part by the E.U. Horizon 2020 Research and Innovation Programme through the Marie Skłodowska-Curie Grant under Agreement 945413 and in part by the Universitat Rovira i Virgili (URV). The work of José Carlos Santos-Ceballos was supported by the Predoctoral Program AGAUR-FI ajuts through the Joan Oró of the Secretariat of Universities and Research of the Department of Research and Universities of the Generalitat of Catalonia and the European Social Plus Fund under Grant 2023 FI-2 00180. The work of Foad Salehnia was supported by the Spanish Ministry of Universities, Recovery, Transformation, and Resilience Plan; and in part by the Maria Zambrano Grant Funded by the European Union—NextGenerationEU under Grant 2021URV-MZ-13. The work of Mohamed Ayoub Alouani was supported by the MICINN under Grant PRE2019-087854. The Associate Editor coordinating the review process was Dr. Gabriele Patrizi. *(Alejandro Santos-Betancourt and José Carlos Santos-Ceballos contributed equally to this work.) (Corresponding author: Foad Salehnia.)*

The authors are with the MINOS, DEEEA, Universitat Rovira i Virgili, 43007 Tarragona, Spain, also with the IU-RESCAT, Research Institute in Sustainability, Climatic Change and Energy Transition, Universitat Rovira i Virgili, 43480 Vilaseca, Spain, and also with the Centre for Environmental, Food and Toxicological Technology (TecnATox), Universitat Rovira i Virgili, 43007 Tarragona, Spain (e-mail: alejandro.santos@urv.cat; josecarlos.santos@urv.cat; foad.salehnia@urv.cat; mohamedayoub.alouani@urv.cat; alfonsojose.romero@urv.cat; joseluis.ramirez@urv.cat; xavier.vilanova@urv.cat).

This article has supplementary downloadable material available at https://doi.org/10.1109/TIM.2024.3481592, provided by the authors.

Digital Object Identifier 10.1109/TIM.2024.3481592

I. Introduction

GAS sensors and their read-out instrumentation systems are essential components in various industry applications due to their crucial role in ensuring safety, enhancing efficiency, and maintaining environmental standards. In different industries such as petrochemical [1] and energy [2], measurement systems interfacing with gas sensors provide reliable data that can prevent dangerous situations such as explosions, toxic exposures, and asphyxiation risks [3], [4]. Likewise, these measurement systems contribute significantly to air quality monitoring by detecting pollutants, enabling industries to comply with environmental regulations and minimize their ecological impact. Similarly, they play a fundamental role in air quality control systems, helping to reduce exposure to harmful substances such as carbon monoxide, nitrogen dioxide, ammonia, and volatile organic compounds in the environment [5].

In past decades, many research efforts have focused on developing reliable gas sensors for detecting pollutant gases. Nowadays, continuous and active research is directed at discovering new materials to increase the response and the selectivity of new sensors [6], [7]. Different gas sensor fabrication techniques such as those based on field effect transistors [8], optical gas sensors [9], and electrochemical sensors [10] have high sensitivity, high selectivity, and fast response time. They also have some downsides such as long-term stability issues. Moreover, their complex designs, fabrication processes, and read-out systems increase the deployment and maintenance costs. On the other hand, chemiresistor gas sensors have emerged as a promising option, as they gather many of the requirements needed in the next generation of low-cost gas sensors. Chemiresistor gas sensors usually show high sensitivity to gases and fast response and recovery times [11], [12]. However, some drawbacks are still challenging, such as the lack of selectivity to specific target gases, temperature and humidity interferences, long-term drift, and high working temperatures [13]. Nontarget gases with similar chemical characteristics can interfere with the gas sensor, especially when detecting mixtures of gases. In addition, sensor drift is a substantial issue, mainly in

outdoor settings when detecting low-concentration levels of analytes. Likewise, the accuracy of chemiresistor gas sensors is directly impacted by environmental variables, as sensor adsorption abilities might vary under the variation of these conditions [14].

A promising area of research to partially solve these issues is the use of chemiresistor sensors such as MOX-based sensors doped or decorated with other materials such as graphene [15], [16] or conductive polymers [17]. Combining this approach with the use of arrays of sensors and multivariate analysis [18], [19] allows the compensation of the interferences that a single sensor might have. The multivariate analysis uses different statistics techniques and machine learning (ML) algorithms [20], [21]. Plenty of methods for the classification and quantification of pollutant gases have been reported, comprising principal component analysis (PCA), linear discriminant analysis (LDA), partial least-squares (PLSs) regression, principal component regression (PCR), decision tree (DT), support vector machine (SVM), k-nearest neighbor (KNN), and artificial neural networks (ANNs) [22], [23], [24].

ML methods have also been used to detect a mixture of gases. Chu et al. [25] identify a mixture of NO_2 and CO in a wide range of concentrations using a sensor array and PCA, BPNN, and CNN. They also evaluate the effect of %RH and compensate for it. Kim et al. [26] used PCA and ANN to recognize a mixture of CO and NH_3 under the presence of NO_2 and recognize NO_2 in the presence of CO and NH_3. Similarly, Zhang et al. [27] used LDA, PCA, and BP-ANN methods to classify CO and CH_4 and their mixture. Also, the authors repeated the experiment by adding interfering species such as H_2 and formaldehyde. All these works and others that can be found in the literature focused on improving feature extraction and data analysis to enhance the classification and quantification output of sensors. They are the groundwork for integrating ML techniques into gas sensing systems. On the other hand, gas sensors have also been integrated into wireless sensor networks (WSNs), estimating the location of gas sources [28], using cutting-edge IoT wireless technologies [29], or being part of distributed devices for air quality monitoring [30], for instance.

We strongly believe that most of these cited features should be integrated into future gas-sensing instrumentation systems to solve the abovementioned issues. This work combines several of these characteristics and applies them to a chemiresistor sensor array developed in our research group. It presents a reconfigurable and adaptative design of an IoT platform at level 4 of the technology readiness level (TRL-4) to detect, classify, and quantify pollutant gases. Details are cited about the fabrication processes of the chemiresistor gas sensors, based on previous experience of our research group, using techniques such as airbrushing [31], [32], laser-induced graphene [33], [34], and aerosol-assisted chemical vapor deposition (AA-CVD) [35], [36]. Also, a full explanation is given about the design of the gas sensor nodes (GSNs), highlighting their versatility as they can interface with all kinds of chemiresistor gas sensors developed in our research group.

In addition, to properly set up the platform, one of the nodes was exposed to different concentrations of ammonia and nitrogen dioxide. Likewise, the percentage of relative humidity was varied, and a mixture of these two pollutants was also sourced to the node. These two gases were chosen due to their crucial role in atmospheric chemistry and the formation of secondary pollutants. On one side, ammonia is largely emitted from agricultural activities [37], including the use of fertilizers [38] and livestock [39]. Nitrogen dioxide, on the other hand, is generally produced from combustion processes, such as vehicle emissions [40] and industrial activities [41]. However, both can be present in places such as agricultural regions near urban or industrial areas. Also, high levels of nitrogen dioxide can often be found inside big cities due to traffic emissions, and ammonia can also be present in urban atmospheres, sourced from waste systems, pets, and some small industrial processes [42], [43]. These emissions are dangerous to human health; exposure to high levels of nitrogen dioxide can irritate the airways in the human respiratory system and aggravate respiratory diseases, such as asthma, increasing episodes of gasping and coughing [44], [45]. Ammonia, while less toxic than nitrogen dioxide, can also irritate the eyes, nose, throat, and respiratory tract upon high exposure levels [46].

A two-stage methodology was established as part of the platform setup process. In stage 1 (training stage), different multilayer perceptron (MLP) ANNs were trained using MATLAB Statistics and ML Toolbox (academic-available license). Then, in the second stage (recognition stage), the obtained MLPs were implemented on the user interface (UI). Repeating this methodology guarantees the reusability of the GSNs with new sensors, the addition of new GSNs to the platform, and the deployment of the platform in different scenarios.

A compilation of systems that use an array of laboratory-made (noncommercial) sensors and support wireless technology found in the literature is summarized in Table I. As shown in Table I, Song et al. [47] perform an indoor deployment of the system but do not consider environmental variables to feed the models. On the other hand, Nath et al. [48] performed an outdoor deployment but did not include ML models in the study. Moreover, Seol et al. [49] incorporated environmental variables but did not add ML models to their results. It is worth noting that this work classifies the type of gas in the atmosphere and quantifies its concentration using ML techniques (in dynamic operation), under a mixture of the target gases, at different percentages of relative humidities; integrating into a platform the aforementioned solutions enhances the output of current gas sensors developed in our research group.

II. Materials and Methods

A. Design and Development of the IoT Platform

The general overview of the platform is depicted in Fig. 1. The platform has three main parts: a server running a Message Queuing Telemetry Transport (MQTT) broker, a UI, and the GSNs interfacing with an array of sensors. A Raspberry Pi was used as a server. Free Eclipse Mosquitto broker was used as the MQTT broker, bridging the raw data from the GSNs to the UI. MQTT is a public-subscribe protocol that

TABLE I
COMPARISON BETWEEN AVAILABLE SYSTEMS AND THIS WORK

Gas	Mix of gases	Hum & Temp	Wireless tech	Classif. algorithm	Quantif. algorithm	Ref
*	[2]	-	BT	PCA/ SVM	[3]	[47]
**	-	-	Wi-Fi	-	-	[48]
NH_3	[4]	-	Wi-Fi	-	-	[50]
H_2S, CO	-	-	BLE/ Wi-Fi	PCA	-	[51]
EtOH	-	Yes	BLE	-	-	[49]
NO_2, NH_3	Yes	Yes	Wi-Fi	ANNs	ANNs	This work

* H_2, formaldehyde, toluene, acetone, ** CH_4, H_2, N_2, [2] indoor deployment, [3] fitting power-law function, [4] outdoor deployment

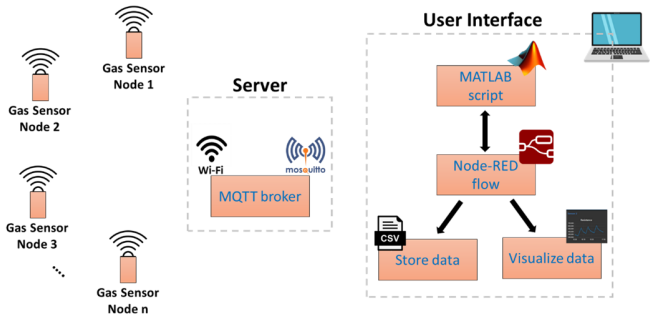

Fig. 1. Block diagram of the IoT platform.

allows the integration of as many GSNs as needed into the platform, facilitating the visualization of the data and multiuser combination. Therefore, new devices could be added to the platform by being subscribed to specific new topics.

The design of the UI was divided into two steps. First, the open-source programming tool Node-RED was used to receive, visualize, and store the data from one of the GSNs. Then, the entire dataset was used to train MLPs (training stage). The second step consisted of creating a new version of the program on Node-RED that uses the previously trained MLPs (recognition stage). To do so, Node-RED communicates with a MATLAB script that preprocesses the sent data from the GSNs and executes the MLPs to quantify and classify the target gas. The GSNs send the raw data from sensors through the MQTT protocol in JSON format (see Fig. S1 in Supplementary Materials). The array of sensors included in the GSNs is formed by a commercially available BME680 sensor (Bosch Sensortec GmbH, Germany) to acquire the humidity and temperature, and four chemiresistor gas sensors (two based on tungsten trioxide, fabricated using AA-CVD technique, and two based on graphene, fabricated by airbrushing and laser-induced graphene techniques). The fabrication process and the characterization of these sensors were previously reported by our research group [31], [32], [33], [34], [35], [36]. Furthermore, Figs. S2–S4 in the Supplementary Materials summarize the fabrication details.

Finally, the GSNs were fully designed in this work. They are wirelessly connected using Wi-Fi technology with the idea

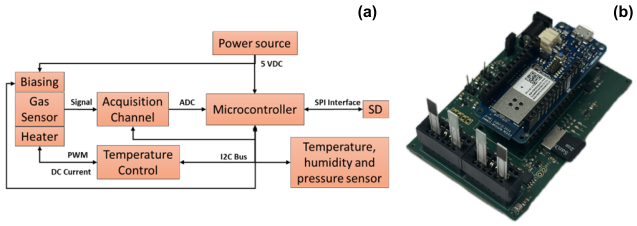

Fig. 2. (a) Block diagram of the GSNs. (b) Final design of the GSNs.

of reusing the extensive coverage of this wireless technology in urban and industrial places. Their main blocks are shown in Fig. 2(a). Key components on the board are the microcontroller, the sensors, the analog acquisition channel, the temperature control circuit, and the power source. The fabricated version of the nodes is shown in Fig. 2(b). It can be noticed that the nodes have a modular design, and an Arm[1] Cortex[1]-M0 32-bit SAMD21 microcontroller (Arduino MKR 1000 Wi-Fi) is connected to the rest of the electronic (green board) through a pin heather connector. This gives the possibility of replacing the MKR 1000 with any pin-compatible MKR-family board to change the type of wireless connectivity according to the final application (e.g., MKR WAN 1300 for LoRa and MKR NB 1500 for narrowband).

The software was also designed in different layers, separating the functionalities related to wireless communication from the other functionalities. Fig. S5 in the Supplementary Materials shows a general flow diagram of the software running in the microcontroller. After loading the start-up configuration, the software performs different control algorithms to guarantee the operation of the sensors connected to the node. The first control algorithm supervises a suitable bias for the sensors in every measurement task. To do so, the biasing circuit continuously checks the value of each sensor and adjusts the bias value using a digital potentiometer (AD5241 I^2C-Compatible 256-Position). This feature compensates for the wide range of baseline resistance values (typically of hundreds of kΩ) that a chemiresistor gas sensor might have and covers up to 1 MΩ. The second control algorithm checks the voltage saturation in the input of the analog-to-digital converter, modifying the gain (if needed) of the measurement channel by changing the feedback resistance of an operational amplifier (using a second digital potentiometer).

Another widely known characteristic of this type of sensor is that most of them require high temperatures to operate [13], [14]. Therefore, the third control algorithm dynamically sets the desired working temperature of the sensor. This is done by repeatedly reading the current through the heater of the sensors using an INA219 Zerø-Drift, Bidirectional Current/Power Monitor with I^2C Interface. This current value is the input of the PID control algorithm. Its output is an increase/decrease of the duty cycle of a pulsewidth modulation (PWM) signal connected to the gate of a p-type MOSFET transistor (NX2301P). The current through the heater can be varied up to 500 mA, covering a wide range of working temperatures. It is worth

[1]Registered trademark.

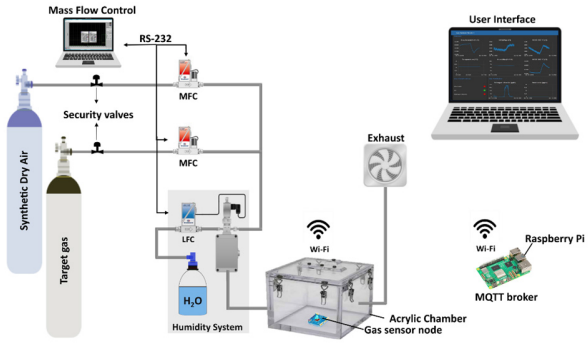

Fig. 3. Schematic of the gas characterization room.

mentioning that the GSNs support up to four chemiresistor gas sensors independently controlled.

The last control algorithm manages the data after a failure/recovery wireless connection. The data would be stored in a μSD memory card if the wireless connection is not established. Once the connection is recovered, the collected data will be sent to the server while simultaneously continuing the data acquisition process. Furthermore, the μSD memory card stores all the start-up and dynamic configurations of the board. Consequently, it is ensured that all the configuration parameters will be unaltered even in the event of a power outage. Finally, the software executes the mentioned algorithms in periodically set tasks such as Read data from sensors and Send data to the server. Sensors are read at a 1-Hz rate, and every 10 s, the average of these values is sent to the server.

B. Gas Characterization Room

The proper working of the platform was tested using one node. The array of sensors in the node was formed by one sensor made of graphene decorated with zinc oxide (Graphene@ZnO) [31], [32], another sensor made of laser-induced graphene decorated with polypyrrole (LIG@Ppy) [33], [34], and the other two sensors were based on pristine tungsten trioxide at two levels of temperatures [35], [36]. The graphene-based sensors were kept at room temperature, while tungsten trioxide sensors were set at 300 °C and 250 °C. It is known in the literature that graphene sensors can work at room temperature, and metal oxide sensors perform better at high temperatures [52], [53]. The node was exposed to different target gases using the system in the gas characterization room illustrated in Fig. 3. The gas measurement system consists of gas bottles with calibrated gas concentrations balanced in dry air, a carrier gas with zero-grade dry air, and an acrylic chamber with an inner volume of 5000 cm^3. The gases were delivered into the chamber through a computer-controlled mass-flow system to ensure a constant low flow of 200 mL/min. The mass flows are controlled by software named Flow Plot v3.34, running on a Windows-based computer. The node was placed inside the chamber and left under dry synthetic air for 3 h to have a stable baseline resistance of the sensors. The data from the four gas sensors and the temperature and humidity sensor were received in Node-RED.

The first set of measurements was established as pulses of nitrogen dioxide, which were injected into the chamber with different concentrations ranging from 100 to 500 ppb incremented by 100 ppb. The second type of measurement targeted ammonia, ranging in concentrations from 10 to 50 ppm incremented by 10 ppm. In both cases, dry air was supplied between the gas pulses to recover the baseline keeping the constant flow. The gas exposure time was 45 min, and the recovery dry airtime was 180 min for each pulse. The cycle of pulses was repeated three times. The humidity level was set by humidifying the gas stream through a controller evaporator mixer from Bronkhorst (Bronkhorst High-Tech, Ruurlo, The Netherlands), and all the described measurements were performed two times under a high humidity level around 65%RH and a low humidity level around 25%RH. Measurements under dry air conditions were not performed because this work focuses on a practical application. Afterward, both gases were injected into the chamber at the same time, exposing the system to a mixture of gases. In this case, the pulses of gases were distributed as follows: five pulses of 25 ppm of ammonia for 90 min and recovery of 3 h and then from 45 to 90 min of each pulse of ammonia; a stream of pulses of nitrogen dioxide was injected as done before 100, 200, 300, 400, and 500 ppb. This cycle was repeated three times. Subsequently, the same procedure was done increasing the ammonia to 50 ppm.

C. Methodology: Training Stage

The following methodology (training stage) was employed to preprocess, train, and test MLPs to classify and quantify the target gases. Fig. S6 in the Supplementary Materials shows the general structure of the MLPs. The electrical resistance of the four gas sensors, along with the data from the temperature and humidity sensor, serves as the input features (input layer) for the training process. First, the array of sensor raw data was filtered using an asymmetric windowed filter with a left–right length of 12 and 0 samples, respectively. Afterward, to transform the values of the features into a common scale (0–1), a min/max normalization technique was used. The normalization process for temperature and humidity sensors was done from 0 °C to 50 °C and from 0%RH to 100%RH. In the case of the gas sensors, the selected range varied according to the resistance values of each baseline. For training, 80% of observations were used, and the remaining 20% were reserved for testing the MLPs, selected randomly for these purposes. A fivefold cross-validation scheme was used to avoid overfitting during the training process. The tuning process compares different types of architecture (hidden layers), varying the number of layers (1, 2, 3) and neurons per layer (10, 25, 100). The MLP with superior performance was selected based on root mean squared error (RMSE) and coefficient of determination (R^2) for quantification and accuracy for classification. Once the architecture of the MLP was fixed, the activation function was varied between ReLU, $f(x) = \max(0, x)$, sigmoid: $f(x) = (1/(1 + e^{-x}))$, and Tanh: $f(x) = (2/(1 + e^{-2x})) - 1$, to decide the best option.

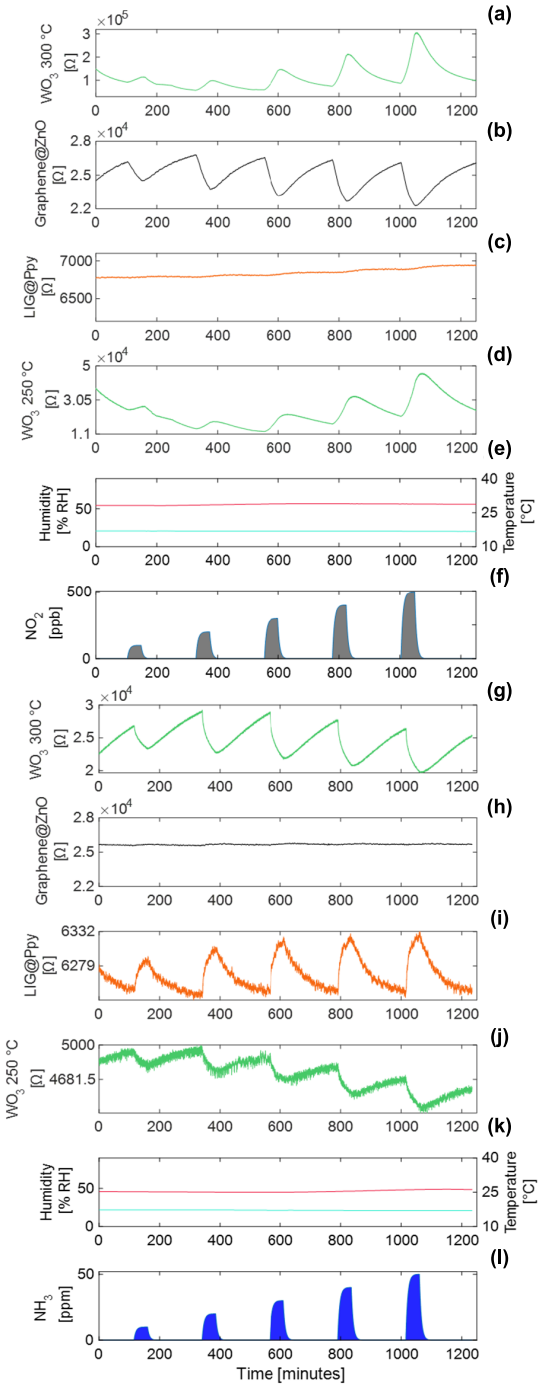

Fig. 4. Temporary response of the sensors to nitrogen dioxide. (a) Tungsten trioxide at 300 °C. (b) Graphene@ZnO. (c) LIG@Ppy. (d) Tungsten trioxide at 250 °C. (e) Temperature and humidity. (f) Nitrogen dioxide pulses: 100, 200, 300, 400, and 500 ppb. Temporary response of the sensors to ammonia. (g) Tungsten trioxide at 300 °C. (h) Graphene@ZnO. (i) LIG@Ppy. (j) Tungsten trioxide at 250 °C. (k) Temperature and humidity. (l) Ammonia pulses: 10, 20, 30, 40, and 50 ppm.

III. Results

A. Gas Sensing Results

The output of the node under nitrogen dioxide exposure is depicted in Fig. 4(a)–(f). Similarly, Fig. 4(g)–(l) shows the output under ammonia exposure.

As noticed in Fig. 4(a), the tungsten trioxide sensor at 300 °C increases its electrical resistance when reacting to nitrogen dioxide. Also, the sensor decreases the electrical resistance of the sensing layer when reacting to ammonia [see Fig. 4(g)]. As expected, the sensor based on Graphene@ZnO decreases its electrical resistance when exposed to nitrogen dioxide [see Fig. 4(b)]. However, there is no change in the electrical resistance when exposed to ammonia [see Fig. 4(h)] [31], [32].

On the other hand, the sensor fabricated using LIG@Ppy presents no variation when exposed to nitrogen dioxide [see Fig. 4(c)] and increases its electrical resistance when exposed to ammonia [see Fig. 4(i)] [33], [34]. Moreover, Fig. 4(d) and (j) depicts the tungsten trioxide sensor at 250 °C. This sensor shows the same behavior as the tungsten trioxide sensor at 300 °C but with lower amplitude variation. It is also noticed that a small drift attributed to the sensor is not fully recovered after the gas exposure due to the lower working temperature. Fig. 4(e) and (k) displays the variation of %RH and temperature in nitrogen dioxide and ammonia scenarios, respectively. Finally, Fig. 4(f) and (l) shows a simulation of the increasing gas concentration inside the chamber, from 10 to 50 ppm (ammonia) and 100–500 ppb (nitrogen dioxide). Note S1 in the Supplementary Materials presents the details of the chosen simulated model [54], [55], [56].

Fig. 5 shows the node output under the exposure of a mixture of ammonia and nitrogen dioxide. The temporary responses of the sensors are depicted in Fig. 5(a)–(e). Fig. 5(f) shows the stream of mixed pulses directed to the sensors, going into the chamber: first 25 ppm of ammonia and then a pulse of increased concentration of nitrogen dioxide. In this manner, a mixture of both gases was ensured in the atmosphere.

A detailed explanation of the waveform variation of the tungsten trioxide sensor at 300 °C is shown in Fig. 6(a). It is noticed that the electrical resistance decreases when the target gas is ammonia (red label number 1). Ammonia is still in the atmosphere when nitrogen dioxide goes into the chamber. The electrical resistance starts increasing (red label number 2). After the pulse stops, the sensor begins recovering, decreasing the electrical resistance (red label number 3). Likewise, Fig. 6(b) shows the response of the graphene-based sensors when both gases go in. First, ammonia goes into the chamber, and LIG@Ppy (plot line in orange color) increases the electrical resistance (red label number 1), while the Graphene@ZnO (plot line in black color) is still recovering from the previous pulse. After the nitrogen oxide goes into the chamber, Graphene@ZnO starts reacting (red label number 2), but the LIG@Ppy continues increasing its electrical resistance even under nitrogen dioxide. Finally, both gases go out from the chamber (red label number 3), and both sensors start recovering their baseline. The same measurements were performed by incrementing the ammonia pulses to 50 ppm, and similar results were obtained.

B. Methodology: Training Stage Results

The MLP employed for gas classification has the output layer of three classification labels: air, ammonia, and nitrogen dioxide. Table S1 in the Supplementary Materials shows the performance of the classification MLPs. The model exhibiting

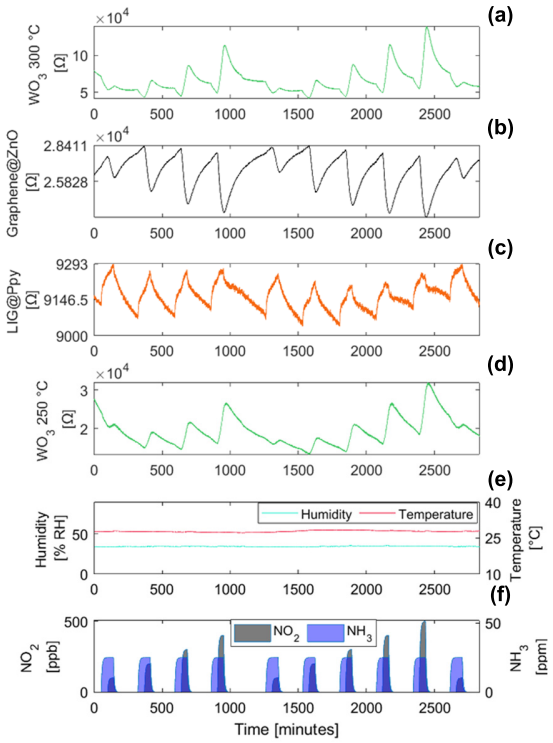

Fig. 5. Temporary response of the sensors under a mixture of ammonia and nitrogen dioxide exposure. (a) Tungsten trioxide at 300 °C. (b) Graphene@ZnO. (c) LIG@Ppy. (d) Tungsten trioxide at 250 °C. (e) Temperature and humidity. (f) Ammonia: 25 ppm mixed with pulses of nitrogen dioxide: 100, 200, 300, 400, and 500 ppb.

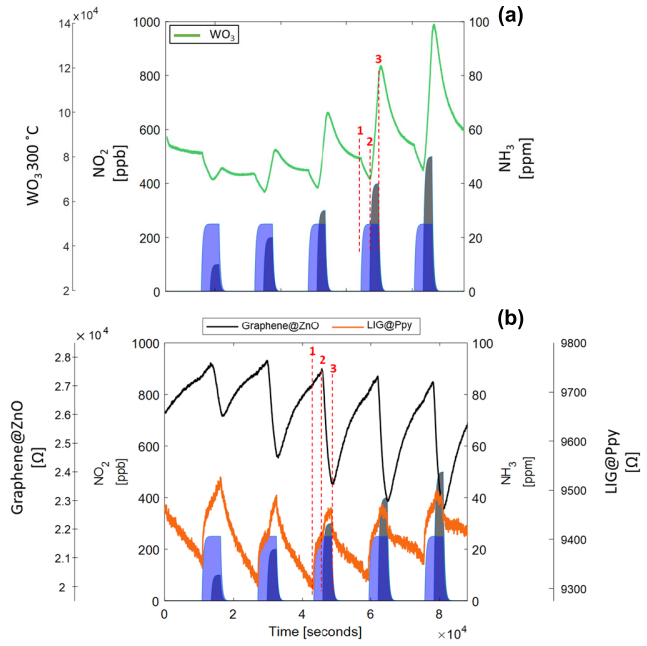

Fig. 6. Temporary response of the sensors under a mixture of ammonia and nitrogen dioxide exposure. (a) Zoomed-in view of the waveform of the tungsten trioxide sensor. (b) Zoomed-in view of the waveform of the graphene-based sensors.

the highest accuracy consists of a single hidden layer with 100 neurons and utilizes Tanh as the activation function. The total accuracy obtained during training (using only the samples

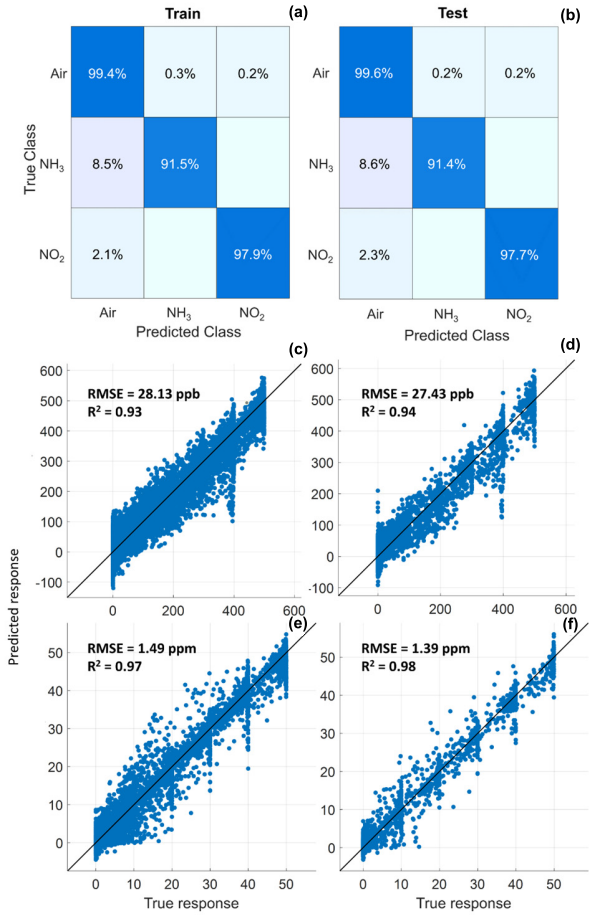

Fig. 7. Confusion matrix for the classification MLP: (a) train data and (b) test data. Results of the best MLP for nitrogen dioxide quantification: (c) train data and (d) test data. Results of the best MLP for ammonia quantification: (e) train data and (f) test data.

of the training dataset) is approximately 98.6%, while, during the test with the observations reserved for this purpose and not used in the training, the total accuracy is 98.7%. Fig. 7(a) and (b) shows the corresponding confusion matrixes. It can be highlighted that the MLP never makes incorrect classifications between target gases. Most of the confusions were observed in the transient response of the sensors between target gas and air. The classification accuracy was greater than 99% when supplying air, 97.9% for nitrogen dioxide, and 91.5% for ammonia. The reason why the classification MLP might have lower accuracy for ammonia is presumed to be due to tungsten trioxide sensors having a higher response to nitrogen dioxide than ammonia.

To understand the influence of temperature and humidity, a classification MLP was trained using only the electrical resistance values of the four gas sensors as input features. In this scenario, the total accuracy of the MLP decreased to 97.6% (train) and 97.4% (test). Notably, in the confusion matrix shown in Fig. S7 in the Supplementary Material, the accuracy of the ammonia classification falls below 90%. This underscores the significance of integrating ambient temperature and humidity as input features into classification MLPs. On the other hand, an MLP was obtained by excluding the

gas sensors with more selectivity to ammonia, LIG@Ppy, and nitrogen dioxide, Graphene@ZnO, resulting in a decrease in accuracy to 95.9% (train) and 96.2% (test). Specifically, ammonia classification dropped considerably to 72%, while nitrogen dioxide classification remained consistent at around 97% (see Fig. S8 in the Supplementary Material). This behavior can be attributed to the good response of tungsten trioxide sensors to nitrogen dioxide, indicating that the absence of the Graphene@ZnO has less influence on the classification of this gas, but is suitable for double-checking the presence of nitrogen dioxide in the atmosphere and avoids mismatches.

Ten quantification MLPs were obtained to quantify the concentration of nitrogen dioxide. Their output layer corresponds to parts per billion (ppb). Table S2 in the Supplementary Materials shows the results. The best MLP was a single hidden layer of 100 neurons, with the ReLU activation function. Fig. 7(c) illustrates the results. In the training process, an R^2 of 0.93 and an RMSE of 28.13 ppb were achieved. In testing, the R^2 score improved slightly to 0.94, with an RMSE of 27.43 ppb [see Fig. 7(d)]. Fig. S9 in the Supplementary Materials demonstrates the impact of temperature and humidity on nitrogen dioxide quantification. Not incorporating these environmental measurements as input features into the quantification model results in R^2 values falling below 0.81 and RMSE values increasing the error above 50 ppb. On the other hand, if LIG@Ppy and Graphene@ZnO are excluded from the quantification MLP, as described in Fig. S10 in the Supplementary Materials, there is an increase in the dispersion of the predicted concentrations compared to the real values. This can be seen in a decrease in the R^2 values, dropping to 0.85, and increases in RMSE more than 45 ppb.

For the prediction of ammonia concentration, quantification algorithms were developed similar to the one used for nitrogen dioxide (see Table S3 in the Supplementary Materials). In these MLPs, the output layer corresponds to the ammonia concentration in parts per million (ppm). Following the mentioned methodology, the best quantification MLP consisted of a hidden layer with 100 neurons and a sigmoid activation function. The results revealed R^2 values of 0.97 (train) and 0.98 (test) [see Fig. 7(e) and (f)] with RMSE values of 1.49 (train) and 1.39 ppm (test). As shown in Fig. S11 in the Supplementary Materials, the quantification MLP trained exclusively with the gas sensors exhibited a minor decrease in the R^2 of 0.96 and an increase in the RMSE of 1.86 ppm. Excluding LIG@Ppy and Graphene@ZnO (see Fig. S12 in the Supplementary Materials) leads to the worst performance of the MLP. R^2 values decrease below 0.90, while RMSE values exceed 3 ppm.

The same methodology was employed to obtain MLPs to classify and quantify the concentrations for a mixture of ammonia and nitrogen dioxide. In the classification process, four distinct labels were defined: air, ammonia, nitrogen dioxide, and mix (indicating the presence of both gases). Table S4 in the Supplementary Materials shows the obtained classification MLPs. The result of the top-performing classification MLP is depicted in Fig. 8(a) and (b), having an accuracy of around 99% for training and testing in most cases. Except

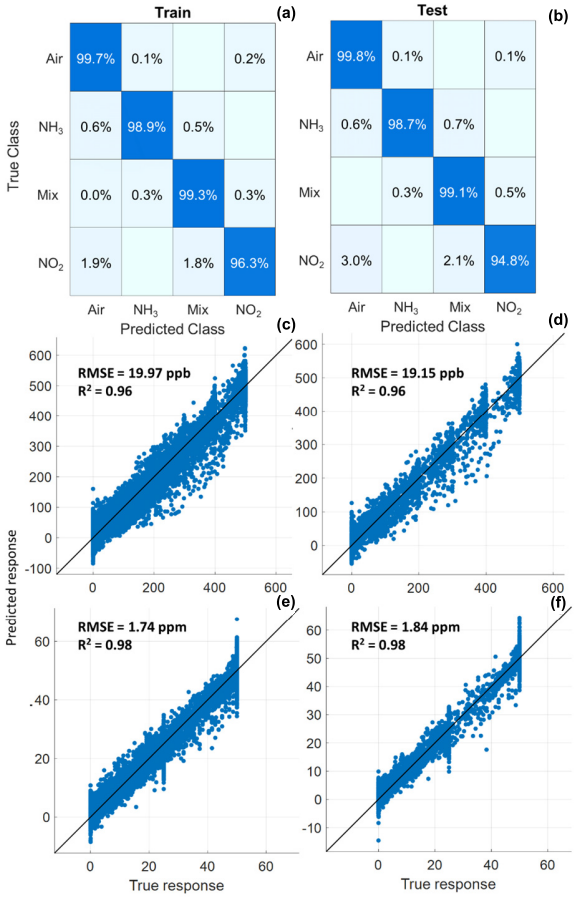

Fig. 8. Confusion matrix of the classification MLP under a mixture: (a) train data and (b) test data. Results of the best MLP for nitrogen dioxide quantification under a mixture: (c) train data and (d) test data. Results of the best MLP for ammonia quantification under a mixture: (e) train data and (f) test data.

when classifying nitrogen dioxide, the MLP was misclassified at 1.9% (train) and 3% (test) with air.

The prediction of the concentration of nitrogen dioxide during a mixture with ammonia exhibited R^2 and RMSE values of 0.96 and 19.97 ppb, respectively [see Fig. 8(c)]. Finally, for quantifying ammonia, the chosen quantification MLP demonstrates favorable performance. The R^2 coefficients stand at 0.98, while the RMSE remains below 1.74 ppm [see Fig. 8(e)]. Tables S5 and S6 in the Supplementary Materials summarize the MLPs of both gases. Fig. 8(d) and (f) shows the test results for nitrogen dioxide and ammonia, respectively.

A summary of the best-obtained classification and quantification models is displayed in Tables II and III, respectively. As noticed, the resultant architectures of the MLPs in both scenarios were the same for the classification and quantification (single layer and 100 neurons per layer). The variation occurred in the selection of the activation function. For classification was selected Tanh (see Table II), for quantifying ammonia, sigmoid, and ReLU for quantifying nitrogen dioxide (see Table III). These results are interesting since ReLU is the most popular activation function for the hidden layers and the first-to-go choice in most neural networks [57]. However, it was only the best in nitrogen dioxide quantification.

TABLE II
SUMMARY OF CLASSIFICATION MLP

HL	N/L	AF	Accuracy train [%]	Accuracy test [%]	Scenario
1	100	Tanh	98.6	98.7	Low and high % RH
1	100	Tanh	99.3	99.2	Mixture of NH_3 and NO_2

TABLE III
SUMMARY OF QUANTIFICATION MLP

Gas	HL	N/L	AF	RMSE train	R^2 train	RMSE test	R^2 test	Scenario
NO_2	1	100	ReLU	28.13 ppb	0.93	27.43 ppb	0.94	Low and high % RH
NH_3	1	100	Sigmoid	1.49 ppb	0.97	1.39 ppb	0.98	
NO_2	1	100	ReLU	19.97 ppb	0.96	19.15 ppb	0.96	Mixture of NH_3 and NO_2
NH_3	1	100	Sigmoid	1.74 ppb	0.98	1.84 ppb	0.98	

HL: number of hidden layers
N/L: number of neurons per layer
AF: activation function

On the other hand, the accuracy, RMSE, and R^2 in both scenarios have similar results. Conversely, when comparing the RMSE on the quantification of nitrogen dioxide, around 1% of the error is incremented under the variation of %RH. This could be attributed to the Graphene@ZnO sensor being more influenced by the variation of %RH than LIG@Ppy.

C. Methodology: Recognition Stage Results

The obtained MLPs were implemented on the UI to test the operation of the IoT platform. While receiving the data from sensors, a MATLAB script is called from Node-RED to classify and quantify the target gases. First, the script receives one by one (as parameters), the raw data from the sensors in each sample period. Furthermore, a preprocessing phase consisted of a FIFO-type buffer, which accumulates 12 values of each sensor and implements an asymmetric left windowed filter [12 0]. Then, after normalizing the values, the classification algorithm is called. Next, it is called the corresponding quantification algorithm using the best MLPs described above. Fig. S13 in the Supplementary Materials shows a screenshot of the UI. The UI has six upper charts related to the raw signal from the four chemiresistor gas sensors and the humidity and temperature sensor. The tree charts at the bottom are the classification and quantification results. Fig. S13(a) presents a 200-ppb pulse of nitrogen dioxide. Likewise, Fig. S13(b) shows a 30-ppm pulse of ammonia, recovery time, and, finally, the beginning of a 40-ppm pulse of ammonia.

In these final measurements, the resultant accuracy was 84.59%, and RMSE and R^2 were 0.97 and 2.33 ppm for ammonia, respectively, and 0.89 and 31.28 ppb for nitrogen dioxide, respectively. These values are in the range of gas-sensing applications found in the literature [58], [59]. It is important to highlight that the implemented gas detection platform improves the quantification response time versus the response time of a single sensor separately. As demonstrated by Llobet et al. [60], [61] and Vilanova et al. [62], the transient response of chemiresistor gas sensors contains relevant information that ANN models can extract. Therefore, the MLPs classify and quantify the gases while acquiring the transient response of the sensors. The MLPs do not wait until the sensors reach the steady state to show a correct output. Fig. 9 shows the details.

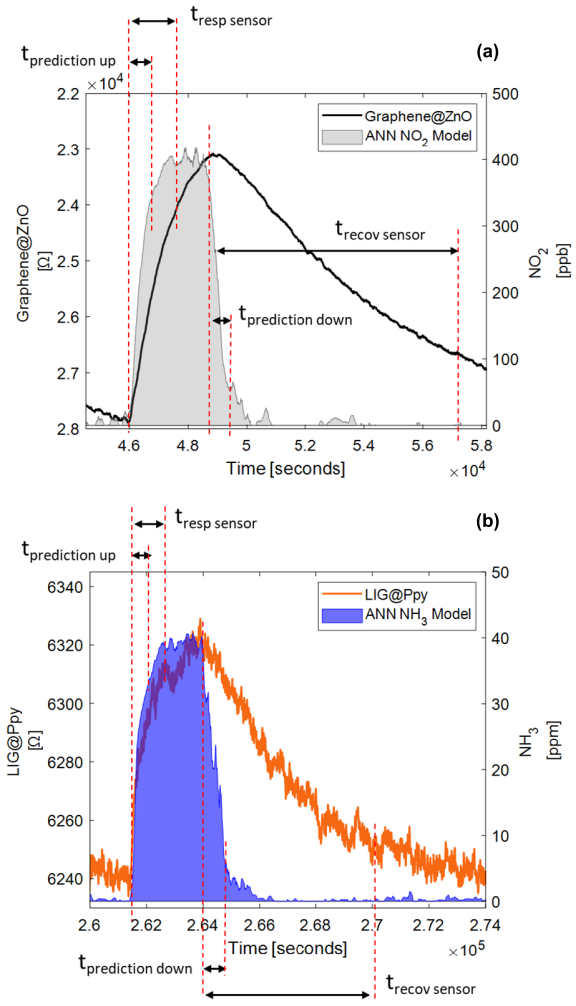

Fig. 9. Comparison of quantification response time between platform and sensor approach. (a) Nitrogen dioxide. (b) Ammonia.

The quantification response time depends on whether the sensors are reacting to the gas or recovering from the reaction. Therefore, from a single-sensor perspective, it is classified into response time ($t_{\_\text{resp sensor}}$) and recovery time ($t_{\_\text{recov sensor}}$). Similarly, from the platform perspective, it is classified into prediction-up time ($t_{\_\text{prediciton-up}}$) and prediction-down time ($t_{\_\text{prediciton-down}}$). The response time and prediction-up time are defined as the time taken to reach 90% of the full response after the exposure of the target gas. The recovery time and prediction-down time are defined as the time taken to reach 90% back of the variation between the steady-state value in the response and the baseline. Fig. 9(a) shows a qualitative comparison between the platform and single-sensor approaches. For nitrogen dioxide, $t_{\_\text{resp sensor}}$ is bigger than $t_{\_\text{prediciton-up}}$.

Also, $t_{\_recov\ sensor}$ is bigger than $t_{\_prediciton\text{-}down}$. A similar result is found when analyzing Fig. 9(b), this time under ammonia exposure. In both cases, the comparison was performed using the selective sensor of each gas, and it was noticed that using the platform reduces the quantification and classification time by around 40% in both cases.

IV. Conclusion

The methodology presented in this work can be used to integrate new chemiresistor gas sensors into the GSNs, add new GSNs to the platform, and deploy the platform in different scenarios. Replacing the sensors for different ones is quickly achievable by repeating the training and recognition stages described during this work. The possibility of reusing low-cost laboratory-made chemiresistor gas sensors in application scenarios raises the versatility of this platform. Using selective sensors increases the probability of discriminating pollutants under a mixture. Furthermore, the platform reduces the classification and quantification time by around 40% (compared with the single-sensor approach). The inclusion of environmental sensors in the GSNs considerably improves the output of the classification and quantification models. As demonstrated in this work, ammonia and nitrogen dioxide were completely classified and quantified under a mixture and at different relative humidity percentages.

The platform has been successfully tested in laboratory conditions and is ready to be deployed in real-application scenarios to update and recalibrate the classification and quantification models (if required). Software and hardware were designed in layers; therefore, it is quite easy to replace the wireless physical layer to tune the platform according to the requirements of the final application. Since communication protocol is based on the MQTT, adding new nodes is as easy as configuring (by software) new topics on the new GSNs to be added. Therefore, deploying this IoT platform in a real-application scenario will be a suitable next step to continue this study.

Acknowledgment

The authors would like to acknowledge the technician of the Minos Group: Xavier Blanch for his help assembling the prototypes.

References

[1] P. Amoatey, H. Omidvarborna, M. S. Baawain, and A. Al-Mamun, "Emissions and exposure assessments of SO_X, NO_X, $PM_{10/2.5}$ and trace metals from oil industries: A review study (2000–2018)," *Process Saf. Environ. Protection*, vol. 123, pp. 215–228, Mar. 2019, doi: 10.1016/j.psep.2019.01.014.

[2] F. M. Adebiyi, "Air quality and management in petroleum refining industry: A review," *Environ. Chem. Ecotoxicol.*, vol. 4, pp. 89–96, Jan. 2022, doi: 10.1016/j.enceco.2022.02.001.

[3] I. Manisalidis, E. Stavropoulou, A. Stavropoulos, and E. Bezirtzoglou, "Environmental and health impacts of air pollution: A review," *Frontiers Public Health*, vol. 8, Feb. 2020, Art. no. 505570, doi: 10.3389/fpubh.2020.00014.

[4] J. González-Martín, N. J. R. Kraakman, C. Pérez, R. Lebrero, and R. Muñoz, "A state-of-the-art review on indoor air pollution and strategies for indoor air pollution control," *Chemosphere*, vol. 262, Jan. 2021, Art. no. 128376, doi: 10.1016/j.chemosphere.2020.128376.

[5] Z. Idrees and L. Zheng, "Low cost air pollution monitoring systems: A review of protocols and enabling technologies," *J. Ind. Inf. Integr.*, vol. 17, Mar. 2020, Art. no. 100123, doi: 10.1016/j.jii.2019.100123.

[6] D. Kwak, Y. Lei, and R. Maric, "Ammonia gas sensors: A comprehensive review," *Talanta*, vol. 204, pp. 713–730, Nov. 2019, doi: 10.1016/J.TALANTA.2019.06.034.

[7] Z. Yunusa, M. N. Hamidon, A. Kaiser, and Z. Awang, "Gas sensors—A review," *J. Environ. Nanotechnol.*, vol. 4, no. 4, pp. 1–14, Dec. 2015, doi: 10.13074/jent.2015.12.153163.

[8] S. Hong et al., "FET-type gas sensors: A review," *Sens. Actuators B, Chem.*, vol. 330, p. 129240, Mar. 2021, doi: 10.1016/j.snb.2020.129240.

[9] J. Li, H. Yan, H. Dang, and F. Meng, "Structure design and application of hollow core microstructured optical fiber gas sensor: A review," *Opt. Laser Technol.*, vol. 135, Mar. 2021, Art. no. 106658, doi: 10.1016/j.optlastec.2020.106658.

[10] D. E. Williams, "Electrochemical sensors for environmental gas analysis," *Current Opinion Electrochem.*, vol. 22, pp. 145–153, Aug. 2020, doi: 10.1016/j.coelec.2020.06.006.

[11] M. L. Grilli, "Metal oxides," *Metals*, vol. 10, no. 6, p. 820, Jun. 2020, doi: 10.3390/met10060820.

[12] R. J. Rath, S. Farajikhah, F. Oveissi, F. Dehghani, and S. Naficy, "Chemiresistive sensor arrays for gas/volatile organic compounds monitoring: A review," *Adv. Eng. Mater.*, vol. 25, no. 3, Feb. 2023, Art. no. 2200830, doi: 10.1002/adem.202200830.

[13] Y.-F. Sun et al., "Metal oxide nanostructures and their gas sensing properties: A review," *Sensors*, vol. 12, no. 3, pp. 2610–2631, Feb. 2012, doi: 10.3390/s120302610.

[14] D. Sales-Lérida, A. J. Bello, A. Sánchez-Alzola, and P. M. Martínez-Jiménez, "An approximation for metal-oxide sensor calibration for air quality monitoring using multivariable statistical analysis," *Sensors*, vol. 21, no. 14, p. 4781, Jul. 2021, doi: 10.3390/s21144781.

[15] D. Sun, Y. Luo, M. Debliquy, and C. Zhang, "Graphene-enhanced metal oxide gas sensors at room temperature: A review," *Beilstein J. Nanotechnol.*, vol. 9, no. 1, pp. 2832–2844, 2018, doi: 10.3762/bjnano.9.264.

[16] X. Tang, M. Debliquy, D. Lahem, Y. Yan, and J.-P. Raskin, "A review on functionalized graphene sensors for detection of ammonia," *Sensors*, vol. 21, no. 4, p. 1443, Feb. 2021, doi: 10.3390/s21041443.

[17] Y. C. Wong, B. C. Ang, A. S. M. A. Haseeb, A. A. Baharuddin, and Y. H. Wong, "Review-conducting polymers as chemiresistive gas sensing materials: A review," *J. Electrochem. Soc.*, vol. 167, no. 3, Sep. 2020, Art. no. 037503, doi: 10.1149/2.0032003JES.

[18] J. Pan et al., "Lightweight neural network for gas identification based on semiconductor sensor," *IEEE Trans. Instrum. Meas.*, vol. 71, pp. 1–8, 2022, doi: 10.1109/TIM.2021.3135503.

[19] L. Zhao, F. Tian, J. Qian, H. Li, and Z. Wu, "Feature ensemble learning for sensor array data classification under low-concentration gas," *IEEE Trans. Instrum. Meas.*, vol. 72, pp. 1–9, 2023, doi: 10.1109/TIM.2023.3251416.

[20] U. Yaqoob and M. I. Younis, "Chemical gas sensors: Recent developments, challenges, and the potential of machine learning—A review," *Sensors*, vol. 21, no. 8, p. 2877, Apr. 2021, doi: 10.3390/s21082877.

[21] M. A. H. Khan, B. Thomson, R. Debnath, A. Motayed, and M. V. Rao, "Nanowire-based sensor array for detection of cross-sensitive gases using PCA and machine learning algorithms," *IEEE Sensors J.*, vol. 20, no. 11, pp. 6020–6028, Jun. 2020, doi: 10.1109/JSEN.2020.2972542.

[22] Z. Ye, Y. Liu, and Q. Li, "Recent progress in smart electronic nose technologies enabled with machine learning methods," *Sensors*, vol. 21, no. 22, p. 7620, 2021, doi: 10.3390/s21227620.

[23] H. Chen, D. Huo, and J. Zhang, "Gas recognition in E-nose system: A review," *IEEE Trans. Biomed. Circuits Syst.*, vol. 16, no. 2, pp. 169–184, Apr. 2022, doi: 10.1109/TBCAS.2022.3166530.

[24] N. Ha, K. Xu, G. Ren, A. Mitchell, and J. Z. Ou, "Machine learning-enabled smart sensor systems," *Adv. Intell. Syst.*, vol. 2, no. 9, Sep. 2020, Art. no. 2000063, doi: 10.1002/aisy.202000063.

[25] J. Chu et al., "Identification of gas mixtures via sensor array combining with neural networks," *Sens. Actuators B, Chem.*, vol. 329, Feb. 2021, Art. no. 129090, doi: 10.1016/j.snb.2020.129090.

[26] J.-Y. Kim, S. P. Bharath, A. Mirzaei, S. S. Kim, and H. W. Kim, "Identification of gas mixtures using gold-decorated metal oxide based sensor arrays and neural networks," *Sens. Actuators B, Chem.*, vol. 386, Jul. 2023, Art. no. 133767, doi: 10.1016/j.snb.2023.133767.

[27] J. Zhang et al., "A miniaturized electronic nose with artificial neural network for anti-interference detection of mixed indoor hazardous gases," *Sens. Actuators B, Chem.*, vol. 326, Jan. 2021, Art. no. 128822, doi: 10.1016/j.snb.2020.128822.

[28] M.-L. Cao, Q.-H. Meng, Y.-Q. Jing, J.-Y. Wang, and M. Zeng, "Distributed sequential location estimation of a gas source via convex combination in WSNs," *IEEE Trans. Instrum. Meas.*, vol. 65, no. 6, pp. 1484–1494, Jun. 2016, doi: 10.1109/TIM.2016.2518358.

[29] S. Ali, T. Glass, B. Parr, J. Potgieter, and F. Alam, "Low cost sensor with IoT LoRaWAN connectivity and machine learning-based calibration for air pollution monitoring," *IEEE Trans. Instrum. Meas.*, vol. 70, pp. 1–11, 2021, doi: 10.1109/TIM.2020.3034109.

[30] S. C. Folea and G. D. Mois, "Lessons learned from the development of wireless environmental sensors," *IEEE Trans. Instrum. Meas.*, vol. 69, no. 6, pp. 3470–3480, Jun. 2020, doi: 10.1109/TIM.2019.2938137.

[31] M. A. Alouani et al., "ZnO-loaded graphene for NO_2 gas sensing," *Sensors*, vol. 23, no. 13, p. 6055, Jun. 2023, doi: 10.3390/s23136055.

[32] A. Santos-Betancourt et al., "ZnO decorated graphene-based NFC tag for personal NO_2 exposure monitoring during a workday," *Sensors*, vol. 24, no. 5, p. 1431, Feb. 2024, doi: 10.3390/s24051431.

[33] J. C. Santos-Ceballos, F. Salehnia, A. Romero, and X. Vilanova, "Flexible sensor utilizing polypyrrole laser-induced graphene nanocomposite for room temperature ammonia detection," in *Proc. IEEE Sensors*, Oct. 2023, pp. 1–4, doi: 10.1109/SENSORS56945.2023.10325068.

[34] J. C. Santos-Ceballos, F. Salehnia, A. Romero, X. Vilanova, and E. Llobet, "Low cost, flexible, room temperature gas sensor: Polypyrrole-modified laser-induced graphene for ammonia detection," *IEEE Sensors J.*, vol. 24, no. 7, pp. 9366–9374, Apr. 2024, doi: 10.1109/JSEN.2024.3368658.

[35] E. Navarrete, C. Bittencourt, P. Umek, and E. Llobet, "AACVD and gas sensing properties of nickel oxide nanoparticle decorated tungsten oxide nanowires," *J. Mater. Chem. C*, vol. 6, no. 19, pp. 5181–5192, May 2018, doi: 10.1039/c8tc00571k.

[36] È. Navarrete et al., "WO3 nanowires loaded with cobalt oxide nanoparticles, deposited by a two-step AACVD for gas sensing applications," *Sens. Actuators B, Chem.*, vol. 298, Nov. 2019, Art. no. 126868, doi: 10.1016/j.snb.2019.126868.

[37] N. Anderson, R. Strader, and C. Davidson, "Airborne reduced nitrogen: Ammonia emissions from agriculture and other sources," *Environ. Int.*, vol. 29, nos. 2–3, pp. 277–286, Jun. 2003, doi: 10.1016/s0160-4120(02)00186-1.

[38] P. Xu et al., "An inventory of the emission of ammonia from agricultural fertilizer application in China for 2010 and its high-resolution spatial distribution," *Atmos. Environ.*, vol. 115, pp. 141–148, Aug. 2015, doi: 10.1016/j.atmosenv.2015.05.020.

[39] C. Ti, L. Xia, S. X. Chang, and X. Yan, "Potential for mitigating global agricultural ammonia emission: A meta-analysis," *Environ. Pollut.*, vol. 245, pp. 141–148, Feb. 2019, doi: 10.1016/j.envpol.2018.10.124.

[40] R. J. Wild et al., "On-road measurements of vehicle NO_2/NO_x emission ratios in Denver, Colorado, USA," *Atmos. Environ.*, vol. 148, pp. 182–189, Jan. 2017, doi: 10.1016/j.atmosenv.2016.10.039.

[41] P. Castellanos and K. F. Boersma, "Reductions in nitrogen oxides over Europe driven by environmental policy and economic recession," *Sci. Rep.*, vol. 2, no. 1, p. 265, Feb. 2012, doi: 10.1038/srep00265.

[42] S. N. Behera, M. Sharma, V. P. Aneja, and R. Balasubramanian, "Ammonia in the atmosphere: A review on emission sources, atmospheric chemistry and deposition on terrestrial bodies," *Environ. Sci. Pollut. Res.*, vol. 20, no. 11, pp. 8092–8131, Nov. 2013, doi: 10.1007/s11356-013-2051-9.

[43] J. N. Cape, Y. S. Tang, N. van Dijk, L. Love, M. A. Sutton, and S. C. F. Palmer, "Concentrations of ammonia and nitrogen dioxide at roadside verges, and their contribution to nitrogen deposition," *Environ. Pollut.*, vol. 132, no. 3, pp. 469–478, Dec. 2004, doi: 10.1016/j.envpol.2004.05.009.

[44] *Air Quality, Energy and Health*. Accessed: Apr. 16, 2024. [Online]. Available: https://www.who.int/teams/environment-climate-change-and-health/air-quality-and-health/health-impacts/types-of-pollutants

[45] *Basic Information About NO_2 | U.S. EPA*. Accessed: Apr. 16, 2024. [Online]. Available: https://www.epa.gov/no2-pollution/basic-information-about-no2

[46] K. E. Wyer, D. B. Kelleghan, V. Blanes-Vidal, G. Schauberger, and T. P. Curran, "Ammonia emissions from agriculture and their contribution to fine particulate matter: A review of implications for human health," *J. Environ. Manage.*, vol. 323, Dec. 2022, Art. no. 116285, doi: 10.1016/j.jenvman.2022.116285.

[47] Z. Song et al., "Wireless self-powered high-performance integrated nanostructured-gas-sensor network for future smart homes," *ACS Nano*, vol. 15, no. 4, pp. 7659–7667, Apr. 2021, doi: 10.1021/acsnano.1c01256.

[48] S. Nath, A. Dey, P. Pachal, J. K. Sing, and S. K. Sarkar, "Performance analysis of gas sensing device and corresponding IoT framework in mines," *Microsyst. Technol.*, vol. 27, no. 11, pp. 3977–3985, Nov. 2021, doi: 10.1007/s00542-019-04621-x.

[49] C. Seok, M. M. Mahmud, M. Kumar, O. J. Adelegan, F. Y. Yamaner, and Ö. Oralkan, "A low-power wireless multichannel gas sensing system based on a capacitive micromachined ultrasonic transducer (CMUT) array," *IEEE Internet Things J.*, vol. 6, no. 1, pp. 831–843, Feb. 2019, doi: 10.1109/JIOT.2018.2861330.

[50] W. Dargie, J. Wen, L. A. Panes-Ruiz, L. Riemenschneider, B. Ibarlucea, and G. Cuniberti, "Monitoring toxic gases using nanotechnology and wireless sensor networks," *IEEE Sensors J.*, vol. 23, no. 11, pp. 12274–12283, Jun. 2023, doi: 10.1109/JSEN.2023.3269723.

[51] J.-H. Suh et al., "Fully integrated and portable semiconductor-type multi-gas sensing module for IoT applications," *Sens. Actuat. B, Chem.*, vol. 265, pp. 660–667, Jul. 2018, doi: 10.1016/j.snb.2018.03.099.

[52] H. Meixner and U. Lampe, "Metal oxide sensors," *Sens. Actuators B, Chem.*, vol. 33, pp. 198–202, Jul. 1996, doi: 10.1016/0925-4005(96)80098-0.

[53] J. Zhang, X. Liu, G. Neri, and N. Pinna, "Nanostructured materials for room-temperature gas sensors," *Adv. Mater.*, vol. 28, no. 5, pp. 795–831, Feb. 2016, doi: 10.1002/adma.201503825.

[54] R. Inglés, J. Pallarés, and J. L. Ramírez, "Improving sample flow in planar preconcentrator," in *Proc. Int. Conf. Comput. Math. Methods Sci. Eng.*, Almería, Spain, Jun. 2010, pp. 1140–1145.

[55] K. Ogata, "Control systems analysis in state space," in *Modern Control Engineering*. Upper Saddle River, NJ, USA: Prentice-Hall, 2010.

[56] D. Laussmann and D. Helm, "Air change measurements using tracer gases: Methods and results. Significance of air change for indoor air quality," in *Chemistry, Emission Control, Radioactive Pollution and Indoor Air Quality*. Rijeka, Croatia: InTech, 2011, doi: 10.5772/18600.

[57] T. Szandała, "Review and comparison of commonly used activation functions for deep neural networks," *Bio-Inspired Neurocomputing*, vol. 903, pp. 203–224, Jan. 2021, doi: 10.1007/978-981-15-5495-7.

[58] M. S. I. Sagar, N. R. Allison, H. M. Jalajamony, R. E. Fernandez, and P. K. Sekhar, "Review–modern data analysis in gas sensors," *J. Electrochemical Soc.*, vol. 169, no. 12, Dec. 2022, Art. no. 127512, doi: 10.1149/1945-7111/aca839.

[59] V. G. Nath, S. P. Bharath, A. Dsouza, and A. Subramanian, "Machine learning algorithms for smart gas sensor arrays," *Adv. Structured Mater.*, vol. 213, pp. 185–225, Apr. 2024, doi: 10.1007/978-981-97-1390-5_8.

[60] E. Llobet, J. Brezmes, X. Vilanova, J. E. Sueiras, and X. Correig, "Qualitative and quantitative analysis of volatile organic compounds using transient and steady-state responses of a thick-film tin oxide gas sensor array," *Sens. Actuators B, Chem.*, vol. 41, nos. 1–3, pp. 13–21, Jun. 1997, doi: 10.1016/s0925-4005(97)80272-9.

[61] E. Llobet, X. Vilanova, J. Brezmes, J. E. Sueiras, and X. Correig, "Transient response of thick-film tin oxide gas-sensors to multicomponent gas mixtures," *Sens. Actuators B, Chem.*, vol. 47, nos. 1–3, pp. 104–112, Apr. 1998, doi: 10.1016/s0925-4005(98)00009-4.

[62] X. Vilanova, E. Llobet, R. Alcubilla, J. E. Sueiras, and X. Correig, "Analysis of the conductance transient in thick-film tin oxide gas sensors," *Sens. Actuators B, Chem.*, vol. 31, no. 3, pp. 175–180, Mar. 1996, doi: 10.1016/0925-4005(96)80063-3.

Alejandro Santos-Betancourt received the Diploma degree in automation engineering from the Technological University of Havana, Havana, Cuba, in 2012, and the M.S. degree from the Microelectronics Research Center, Havana, in 2017.

He is currently involved in a Ph.D. Program at the Technologies for Nano-Systems, Bioengineering, and Energy, Universitat Rovira i Virgili, Tarragona, Spain. His research interests are wearable electronics, IoT, wireless, and embedded systems.

José Carlos Santos-Ceballos received the B.S. degree in automatic engineering and the M.S. degree in digital systems from the Universidad Tecnológica de La Habana "José Antonio Echeverría," CUJAE, Havana, Cuba, in 2015 and 2020, respectively. He is currently pursuing the Ph.D. degree with the Department of Electronic, Electrical and Automatic Control Engineering, Universitat Rovira i Virgili, Tarragona, Spain.

From 2015 to 2022, he was an Electronic Design Specialist at the Development Department of the Cuban Center for Neuroscience, Havana. His research interests include wearable gas sensors, signal processing for gas sensing, and embedded systems.

Foad Salehnia was born in Sanandaj, Iran. He received the Ph.D. degree in nanochemistry from the University of Tehran, Tehran, Iran, in 2019.

He subsequently completed two postdoctoral positions at the University of Tehran. He is currently a Maria Zambrano Research Fellow at the MINOS Research Group, University of Rovira i Virgili, Tarragona, Spain. His research interests focus on synthesizing novel carbon-based nanomaterials and investigating their applications in sensing areas and energy conversion systems.

Mohamed Ayoub Alouani received the B.S. degree in chemistry and the M.S. degree in solid state chemistry from the Faculty of Sciences, University of Tunis el Manar, Tunis, Tunisia, in 2017 and 2019, respectively. He is currently pursuing the Ph.D. degree with the Department of Electronic, Electrical, and Automatic Control Engineering, Universitat Rovira i Virgili, Tarragona, Spain.

His research is focused on the technologies of nanosystems, bioengineering, and energy, and the synthesization and characterization of 2-D nanomaterials and mixing with graphene for gas sensing at room temperature.

Alfonso Romero received the Ph.D. degree from the Universitat Politecnica de Catalunya (UPC), Barcelona, Spain, in 2001.

He is an Associate Professor of electronics technology at the Universitat Rovira i Virgili, Tarragona, Spain. His research interests comprise instrumentation electronics applied to electronic sensor measurements and data transmissions.

José Luis Ramírez was born in Reus, Spain, in 1970. He received the Telecommunications Engineering and Ph.D. degrees in analog microelectronic design from the Universitat Politècnica de Catalunya, Barcelona, Spain, in 1994 and 2003, respectively.

He is currently an Associate Professor at the Universitat Rovira i Virgili, Tarragona, Spain. His main research topics are related to transducers for sensing microsystems, digital/analog microelectronics, and microcontroller-based designs.

Xavier Vilanova received the Ph.D. degree from the Universitat Politecnica de Catalunya (UPC), Barcelona, Spain, in 1998.

Since 2010, he has been a Full Professor of electronics technology at the Universitat Rovira i Virgili, Tarragona, Spain. His research interests comprise gaining insight into the information extracted from gas sensor transients when exposed to pulsed light excitation. He is also working on developing scalable and low-cost processes to obtain flexible gas sensors.